On the equilibrium morphology of systems drawn from spherical collapse experiments

C. M. Boily[1,†] & E. Athanassoula[2]

[1] *Observatoire astronomique de Strasbourg, 11 rue de l'université, 67000 Strasbourg, France*
[2] *Observatoire de Marseille, 2 Place Le Verrier, 13248 Marseille Cédex 4, France*
[†] *Formerly at: Astronomisches Rechen-Institut, Mönchhofstrasse 12-14 Heidelberg, D-69120 Germany*

2005 April 15

ABSTRACT

We present a purely theoretical study of the morphological evolution of self-gravitating systems formed through the dissipation-less collapse of N point sources. We explore the effects of resolution in mass and length on the growth of triaxial structures formed by an instability triggered by an excess of radial orbits. We point out that as resolution increases, the equilibria shift, from mildly prolate, to oblate. A number of particles $N \simeq 100,000$ or larger is required for convergence of axial aspect ratios. An upper bound for the softening, $\epsilon \approx 1/256$, is also identified. We then study the properties of a set of equilibria formed from scale-free cold initial mass distributions, $\rho \propto r^{-\gamma}$; $0 \leqslant \gamma \leqslant 2$. Oblateness is enhanced for initially more peaked structures (larger γ's). We map the run of density in space and find no evidence for a power-law inner structure when $\gamma \leqslant 3/2$ down to a mass fraction $\lesssim 0.1\%$ of the total. However when $3/2 < \gamma \leqslant 2$ the mass profile in equilibrium is well matched by a power-law of index $\approx \gamma$ out to a mass fraction $\approx 10\%$. We interpret this in terms of less effective violent relaxation for more peaked profiles when more phase mixing takes place at the centre. We map out the velocity field of the equilibria and note that at small radii the velocity coarse-grained distribution function is Maxwellian to a very good approximation.

We extend our study to non-scale-free initial conditions and finite but sub-virial kinetic energy. For cold collapses the equilibria are again oblate, as the scale-free models. With increasing kinetic energy the equilibria first shift to prolate morphology and then to spherical symmetry.

Key words: numerical method: N-body; galaxies, gravitational dynamics

1 Introduction

This is a purely theoretical investigation into the formation of equilibria reached through a phase of gravitational collapse (Lynden-Bell's [1967] violent relaxation process) using numerical N-body calculations. Our motivation for this undertaking is drawn both from observations and theory, as discussed first below. A survey of recent work in that area follows.

1.1 Cusps in triaxial galaxies

HST images of elliptical galaxies have revealed cuspy ($\rho \propto r^{-\gamma}$) density profiles down to resolution limits (e.g., Lauer et al. 1995; Gebhardt et al. 1996; Laine et al. 2003). Fits to their luminosity profiles indicate power-law indices ranging from $\gamma \approx 1/2$ to $\gamma \approx 2$. These observations have triggered several studies of the origin and orbital content of singularities at the heart of galaxies. The orbital structure of cuspy

triaxial galaxies would harbour a broad range of resonant and near-resonant orbits, including also chaotic orbits (e.g., Merritt & Fridmann 1996; Holley-Bockelmann et al. 2001). Whether or not the cusp hosts a massive (single or binary) black hole affects both the orbital families that support the cusp as well as the overall mass profile (Holley-Bockelmann et al. 2002; Poon & Merritt 2001; Nakano & Makino 1999; Merritt & Cruz 2001). Furthermore, the diffusion of chaotic orbits in cuspy potentials may lead to a rapid readjustment of the equilibrium (Merritt & Fridman 1996; Kandrup & Siopis 2003). Thus the possibility of tracking individual orbits in self-consistent potentials can hand diagnostics on the stability of ellipticals and on the demographics of black holes in galaxies.

In this contribution, we construct cuspy triaxial galaxies obtained from the classic initial-conditions problem of violent relaxation. In particular we are interested in the numerical resolution of central density peaks and, at large radii, the global morphology in equilibrium. Analytic and semi-

analytic models of triaxial galaxies can be constructed from distribution functions subject to appropriate constraints (see e.g., Dehnen & Gerhard 1994; Holley-Bockelmann et al. 2001; van de Ven et al. 2003). However, we chose the flexible three-dimensional N-body approach to explore a range of initial conditions and study the time-evolution of the systems. This allows total freedom with regard to the symmetry and boundary conditions imposed on the system. Drawbacks include finite spatial and mass resolution imposed by limited computer resources. This calls on us to check which simulations parameters allow sufficient accuracy and convergence in the numerics, with a view to develop a full library of non-analytic models in the most cost-efficient way.

We divide our study in two parts. This contribution is the first part devoted largely to checks of the numerical setup and a parameter survey. In a forthcoming contribution we will explore the families of orbits and derive observables from the equilibria obtained. Here, first we define the initial conditions for collapse in terms of an accretion problem and give details of the numerical method (§2). Drawing from known correlations between equilibrium and initial energy distributions (van Albada 1982; Aguilar & Merritt 1990; Henriksen & Widrow 1999) we setup sub-virial scale-free power-law mass profiles ($\propto r^{-\gamma}$; see Eq.[1] below). We monitor the convergence of physical parameters (axis ratios, density profiles) with particle number, N, and linear resolution ϵ in §3. We then relate equilibrium properties to the initial conditions in terms of mass profile and virial ratio (see §3 and §4), with the expectations that the power-index of the inner density profile will match γ of the initial conditions. The properties of a set of cuspy density profiles are worked out for γ in the range $0 \leqslant \gamma \leqslant 2$, covering the range of power indices derived for observed ellipticals (§5 and §6). We conclude with an extended discussion and possible applications of these results in a cosmological context. A brief survey of the literature on the topic of violent relaxation is helpful to set our goals in context.

1.2   Previous numerical work on violent relaxation

In a ground-breaking N-body numerical investigation of violent relaxation, van Albada (1982) showed that the de Vaucouleurs $R^{1/4}$ projected luminosity profile of ellipticals could be understood as the outcome of gravitational collapse. This feature proved attractive since massive ellipticals are largely pressure-supported with little net rotation (Davies et al. 1983; Binney & Merrifield 1999), a by-product of violent relaxation (e.g. May & van Albada 1984; Curir & Diaferio 1994). Later, radial orbit instabilities (ROI) were shown to develop in numerical renditions of anisotropic systems constructed from equilibrium distribution functions $f(E, J^2)$ of energy and square angular momentum (Merritt & Aguilar 1985; Barnes, Hut & Goodman 1986) as well as in the end-results of violently relaxed systems (Aguilar & Merritt 1990; Canizzo & Hollister 1992). The ROI develops in e.g. collapsing (sub-virial) spherical distributions due to large radial bulk motion, so that the initial symmetry is lost and the systems become triaxial in equilibrium. The aspect ratios (of mean $\sim 1 : 2$ [E5]) attained in these studies cover the entire spectrum of ellipticals. Aguilar & Meritt (1990) demonstrate that the equilibrium distribution functions f satisfies Antonov's stability to radial perturbations $\partial f/\partial E < 0$,

where E is the binding energy. However, van Albada's low-resolution core-halo equilibria makes direct application of these results to the inner structure of cuspy de Vaucouleur and HST galaxies less than straightforward. It was noted that relaxation from less smooth (clumpy) initial conditions leads to more compact virialised equilibria (e.g. McGlynn 1984; Aguilar & Merritt 1990; Roy & Perez 2004) possibly offering a way forward[1]. In the late 1980's the emphasis on galaxy formation shifted to include gas cooling and the transformation of spirals to ellipticals through mergers (see e.g. Barnes & Hernquist 1992). Dissipation-less dynamics with N-body calculations recast in the framework of hierarchical structure formation in a CDM cosmogony was found to give rise to equilibria with steep central cusps ($\gamma \gtrsim 1$: Navarro et al. 1997, 2004; Fukushige & Makino 1997, 2001; Fukushige, Kawai & Makino 2004; Moore et al. 1998, 2004; Diemand et al. 2005). Thus repeated episodes of mass accretion would seemingly lead to equilibria with steeper central cusps.

Both Aguilar & Merritt (1990) and Canizzo & Hollister (1992) modelled sub-virial mass in-fall with power-law initial mass profiles distributed spherically. Each mass shell collapses to the origin at a different time, and the accretion is continued until the last mass shell converges to the origin. They have shown that (1) the ensuing equilibria are highly prolate; (2) the aspect ratio (defined from the eigenvectors of the inertia tensor) increases radially and is near unity at large radii; (3) the spherically-averaged density profiles of equilibrium systems correlates with the initial profile. These investigations were carried out using multi-polar series expansion and the TREE (Barnes & Hut 1986) integrators respectively with $N = 5,000$ and $10,000$ mass elements. More recent work by Roy & Perez (2004) used up to $N = 30,000$ particles. One important result drawn from this study is that homogeneous initial mass profile lead to equilibria that match better cored globular cluster in equilibrium, a conclusion that lends support to the analysis of LMC clusters of Boily et al. (1999).

The current, purely theoretical study must be cast in the context of the interesting, full-fledged parameter survey of Roy & Perez to highlight differences :

1) Recently we have shown that collapse factors in spherical symmetry are indistinguishable from those obtained from non-spherical in-fall when the mass resolution $N \lesssim 10^5$ (Boily et al. 2002 $\equiv$ BAK+02). This raises issues with the growth of velocity anisotropies near the time of maximum contraction in studies with lower resolution. Aarseth et al. (1988) and Hozumi et al. (1996) have argued that the tangential velocity dispersion grows faster than the radial component at the bounce. Tangential velocities will arise from the growth of fragmentation modes (McGlynn 1984; Aarseth et al. 1988). Clearly the velocity field must develop fully for numerical convergence of the end-product properties. The results of BAK+02 would suggest a minimum $N \approx 10^5$ in order to discriminate between spherical and non-spherical growth modes, by resolving the dynamics at maximum contraction well. We confirm in §4 that nu-

---

[1] The same holds if a smooth collapsing system has random tangential velocities initially (Hozumi et al. 2000; LeDelliou & Henriksen 2003).

merical convergence is reached when N falls in this range of values.

2) Any cold isotropic distribution of mass develops clumps at the onset of collapse. Roy & Perez (2004) seeded some of their initial mass distributions with homogeneous clumps (also spherically symmetric). Such initial conditions are difficult to duplicate for non-homogeneous spheres as done here owing to the tidal force of the background potential which does not define a spherical Roche boundary. For that reason, we limit our study to distributions of point sources with no internal degrees of freedom. This is only a minor setback however because clumps that form in our simulations during in-fall grow self-consistently from Poisson (root-n) seeds. These small clumps merge as in-fall proceeds which lead to the growth of a few large clumps just prior to maximum in-fall (see e.g. Fig. 7 of Aarseth, Lin & Papaloizou 1988). Thus the full process is highly *anisotropic despite* the choice of spherically symmetric initial conditions.

3) Roy & Perez (2004) considered finite-Q (their parameter η) initial conditions only; we will show that the limit where $Q \to 0$ gives rather different equilibria. In that sense, our survey complements theirs while focusing on more specific initial conditions.

It may be worth commenting that while we chose power-law initial conditions to generate power-law equilibria, an expectation drawn from past experiments with initial value problems of this kind, we found surprisingly that power-laws are recovered only for a sub-set of the parameter space, a result that turns on its head the long-held belief that the phase-space structure in equilibrium correlates strongly with the initial conditions chosen. While correlations are found, the end-results do differ significantly from those anticipated.

All numerical studies using particle-based methods have used the virial ratio Q as a free parameter. This is partly justified on the grounds that there may not exist unique diagnostics for the growth of ROI either in terms of a critical Q or a global anisotropy parameter in a spherical equilibrium (Palmer & Papaloizou 1987; Perez et al. 1996; see Merritt 1999). Generally lower values of Q lead to deeper radial infall and more anisotropic velocity fields in equilibrium (more radial orbits), which favours ROI[2]. Henriksen & Widrow (1997) have shown using a one-dimensional code that orbit-crossing which develops during in-fall leads to self-similar patterns which break off through a phase-mixing instability. Rapid phase-mixing softens the regime of violent relaxation that then sets in. Merral & Henriksen (2003) argue that this instability will develop more slowly when $Q > 0$. Consequently the similarity pattern persists longer in those cases. We will address this point in a study of three-dimensional 'warm' collapses by comparing their outcome with those of cold collapses.

2 Method

2.1 Initial conditions

2.1.1 Cold collapses

Similarly to other authors (Aguilar & Merritt 1990 $\equiv$ A&M+90; Cannizzo & Hollister 1992 $\equiv$C&H+92; Henriksen & Widrow 1997) we setup a series of spherically symmetric cold scale-free distributions of mass density

$$\rho_o(r) \propto (r/r_s)^{-\gamma} \qquad (1)$$

with $0 \leqslant \gamma < 5/2$. The lower limit corresponds to homogeneous spheres; the upper bound corresponds to systems with finite gravitational binding energy $GM^2/r \propto r^{5-2\gamma}$. Notice that all models with $\gamma > 1$ have a diverging force field at the centre. A value of $\gamma = 3/2$ was adopted as reference for the setup of the numerics and convergence of the parameters. The full range of models is listed in Table 1.

2.1.2 Scaling the velocities with Q

In order to assess how warm initial conditions influence equilibrium profiles, we ran also a few simulations in which the particles did not start from rest. Instead, they proceed from Dehnen (1993) density profiles and matching velocity field. The density profile of these models is given by

$$\rho(r) = \frac{(3-\gamma)\, M}{4\pi} r^{-\gamma} \frac{r_0}{(r_0 + r)^\beta}, \qquad (2)$$

where γ fixes the inner power-law index, $\beta = 4 - \gamma$, r_0 and M are constants fixing the scales of length and total system mass. Because of known correlations between initial conditions and equilibria through incomplete relaxation (cf. §1.1), we expect initial- and equilibrium power-indices of the mass profiles near the centre to be equal. Of all the Dehnen models the one with $\gamma = 3/2$ gives the best match to a de Vaucouleur profile, as the reference power-index value adopted for cold collapses.

We define the system virial ratio of kinetic to gravitational energy, Q, as

$$Q \equiv \frac{2M\sigma^2}{W} \qquad (3)$$

where σ is the three-dimensional velocity dispersion (we consider only irrotational models). $Q = 1$ for a virialised equilibrium, whereas $Q < 1$ ensures that all shells of constant mass converge to the barycentre of the system. Several studies of gravitational collapse assign particle velocities randomly (e.g. McGlynn 1984; A&M+90; C&H+92; Boily et al. 1999). In the present study, however, we assign velocities from the equilibrium distribution function as follows. The gravitational binding energy W is computed directly from (2) while the global mean square velocity dispersion σ^2 is obtained from the Jeans equation in spherical symmetry (Binney & Tremaine 1987, §4.2).

We then attribute velocities according to an isotropic Maxwellian velocity distribution constrained to satisfy locally the first three moments of the Boltzmann equation. The velocities are then renormalised to achieve the desired

---

[2] The ROI is a Jeans type of instability developing in equilibrium systems. The two-stream instability (in- and out-flow) may provide a more appropriate description of the outbreak of a bar during in-fall; see Barnes, Hut & Goodman (1986).

global virial ratio Q in (3). This approach has the advantage that the velocities are self-consistent with the mass profile of the system, and follows the strategy adopted by Barnes et al. (1986) in their study of the growth of ROI's in equilibrium systems.

2.2   Choice of integration parameters

2.2.1   Choice of units

Power-law distributions were all truncated at a fixed radius $r_t = 2$. We adopted units such that $G = M = 1$, which, together with r_t, sets all scales in the problem. For an initial density profile $\rho(r) = \rho_o(r/r_s)^{-\gamma}$, the scales of length r_s and of density ρ_o satisfy $\rho_o r_s^\gamma = (3 - \gamma)/4\pi M r_t^{\gamma-3} = 2^{\gamma-3}(3 - \gamma)/4\pi$.

2.2.2   Time-step and free-fall time

The evolution of the N-body models was followed on the Marseille Grape-5 systems (Kawai et al. 2000), using a specially adapted TREE-code (Athanassoula et al. 1998). The code uses a fixed time-step which we set equal to

$$\delta t = t_{\rm ff}/3000$$

where the nominal free-fall time, $t_{\rm ff}$, is

$$t_{\rm ff} \equiv \sqrt{\frac{3\pi}{32G\langle\rho\rangle}} \qquad (4)$$

where $\langle\rho\rangle = M/(4\pi r_t^3/3)$ is the mean density. In computing units $t_{\rm ff} \simeq 3.07(0)$.

Direct application of the virial theorem ($r \simeq r_t/2$) at constant M means that the system crossing time in equilibrium $t_{cr} = 2r/\sigma_{1d} = 2/\pi\, t_{\rm ff} \simeq 0.637\, t_{\rm ff}$ will take a value close to half the free-fall time, or 1.95(6) N-body time units; we will use $t_{cr} = 2$ N-body time units for convenience when discussing the results. The code uses a Plummer smoothing ϵ

$$\phi(r) \equiv \frac{GM}{\sqrt{r^2 + \epsilon^2}}$$

to avoid divergences due to particle-particle interactions. The nature of the problem at hand requires a careful setup to ensure that global energy and angular momentum are preserved to good accuracy throughout evolution. The maximum relative error $\delta E/E$ (in percentage) measured during the complete evolution fluctuates between different runs, but remains of the order of, or better than, a few parts in a thousand for the adopted values of the opening angle, softening and time step. We discuss these values briefly.

2.2.3   Choice of softening ϵ

As in all cases, the value of ϵ should be tailored to the problem at hand. The softening must be large enough to avoid collisions between particles, while being small enough to resolve time-variations in the potential at all stages of evolution. Our problem is particularly difficult, since it includes both very high density and very low density regions. Furthermore, particles do not stay all through the evolution in regions of similar density, but can visit regions of very different density.

We tried a number of softening lengths ranging from 1/32 to 1/1024 and after many tests, some of which are described in section 4, we adopted a reference smoothing length of 1/512. The effect of changing this value and how this influences results are discussed in section 4.3.

Of course we can not trust our results for distances smaller than a few times the softening length. In practice we took a conservative radius of $5 \times \epsilon$ as the inner-most radius to compute physical parameters (velocity dispersion, density, etc).

2.2.4   Choice of opening angle θ_c

The TREE method defines a critical angle θ_c to control the accuracy of a limited expansion to the force field. The choice of θ_c is a compromise between high accuracy and performance. In most simulations an opening angle $\theta_c \approx 0.7$ allows energy conservation typically to the order of 0.1% (Barnes & Hernquist 1996; Athanassoula et al. 2000). For collapse calculations, however, as for mergings, the time-variations of the potential are rapid and large, so such an opening angle may not necessarily suffice. We have thus carried out a series of calculations varying θ_c and Plummer softening to determine which combination of parameters allows integration to the desired accuracy. Our results proved robust for a wide range of opening angles (cf. Fig. 5). We adopted a median value $\theta_c = 0.4$ for all our calculations. Simulations with an opening angle of 0.7 give a somewhat larger value of the energy variation. We thus did not include them in the analysis presented in the next sections. In general, runs that gave energy errors larger than 1% were discarded from analysis altogether.

2.3   Physical description

Starting with zero kinetic energy, all particles converge toward the centre of gravity which coincides with the centre of coordinates. Since the free-fall time

$$t_{\rm ff} \propto \frac{1}{\sqrt{G\langle\rho\rangle}} \propto (r/r_s)^{\gamma/2} \qquad (5)$$

increases with radius, several orbits cross at the centre before a significant fraction of the mass has reached there. This feature allows us to treat the problem as an accretion problem. At constant radius, the flux of matter through a shell during in-fall

$$\dot{m} = 4\pi r^2 \rho(r,t) v_r(t) \propto r^{3-3\gamma/2} \propto t^{3(2-\gamma)/\gamma} \qquad (6)$$

increases with time when $\gamma \leqslant 2$. The above relation was derived by following an in-falling shell of constant internal mass and so holds up to first orbit crossing. As orbits begin to cross at the centre, a pattern emerges from the origin and propagates outwards. At a given radius, out-going particles eventually meet with in-falling material and the net mass in-flux $\dot{m}$ drops. Thereafter a self-consistent equilibrium is established over some ≈ 20 N-body units of time (or, $\approx 10\, t_{cr}$); all our simulations ran for 80 N-body units of time, or ≈ 40 dynamical times, to ensure stability of the

equilibrium configurations. Note that the classical two-body relaxation time at the system half-mass radius, t_{rh}, is given by (see Binney & Tremaine 1987)

$$\frac{t_{rh}}{t_{cr}} \simeq \frac{1}{10} \frac{N}{\ln 0.4N}$$

so that for $N = 100,000$ particle calculations $t_{rh} \approx 900 \, t_{cr}$ is much larger than the total runtime of the simulations. In fact, the *central* relaxation time, defined in terms of the dynamical time at the centre, can accommodate an t_{cr} shorter by a factor 20, or an increase in density of $20^2 = 400$, and still remain clear of two-body relaxation effects. We checked explicitly for several cases that runs with this number of particles did not exceed a density contrast (central to half-mass values) of 100 (cf. Fig. 1). We have performed a few runs with particle number $N \sim 10^4$, to ease comparison with results from previous papers where this value of N was used. Runs with $N \sim 10^4$ have $t_{rh} \sim 160 \, t_{cr}$ at the half mass radius; the maximum density contrast allowed is now $\simeq 16$, close to what was obtained (Fig. 1). These runs will likely have suffered a degree of two-body relaxation at the centre : to ensure that our analysis was not affected by relaxation for this case, we also took snapshots at time $t = 40$ (half the evolution time) and verified that very similar conclusions applied. Therefore only results obtained for $t = 80$ units of evolution will be presented. We note that the relaxation time estimates are conservative since they do not take account of softening. This cuts off large-deflection angle encounters and lengthens collisional relaxation (see e.g. Theis & Spurzem 1999; Athanassoula, Vozikis & Lambert 2001).

3 Example : time-evolution of an $\gamma = 3/2$ run

3.1 Centre of density vs centre of mass

Gravitational collapse leads to a spread of the individual particle energy range. Particles acquiring positive energy leave the system on a dynamical time-scale. Overall, on the order of 10% of the particles escape. The fraction of escapers is a function of both accretion index γ and initial morphology. The combined effects may cause up to $\approx 22\%$ mass loss for homogeneous spherical systems (Table 1 of C&H+92; Boily 1994). As a result of the growth of radial orbit instability and of anisotropic loss of unbound particles, the centre of coordinates does not necessarily match the centre of mass of the bound particles. We found in most cases a small but non-zero linear momentum carried away by escapers. In all the analysis, and in particular when fitting isodensity curves and calculating the inertia tensors and their eigenvalues, we recentered the coordinates to the center of density (i.e. the maximum density point) in order to avoid errors due to off-centered isophotes. The density maximum was identified using the six-nearest neighbour scheme of Casertano & Hut (1985). The approach allows a much higher resolution of density profile around the centre, down to a few $\times \epsilon$ (Fig. 1). The NEMO package utility functions greatly helped automate the procedure (see http://bima.astro.umd.edu/nemo/; Teuben 1995).

3.2 Inside-out morphology

We investigated the morphology of equilibrium profiles in the centre of density frame in two different ways. First we sorted the particles in binding energy and removed the 20% particles with the largest energy (which includes all unbound particles). We then divided the remaining particles in four bins, each containing 20% of the initial particle number. In this manner we did not take into consideration unbound particles and particles bound to the system but in a very-low density region: this imitates the effect of a tidal boundary. We also used an alternative approach, which consisted in sorting particles by increasing spherical radius and removing the outermost 20%. In both cases we re-centered on the density maximum of the remaining particles. The two approaches gave similar results.

We computed the inertia tensor of selected particles, separately for each bin. The orientation of the system was set so that Cartesian axes matched the principal axes of the bound particles, with the positive x-axis coinciding with the semi-major axis. We then defined ellipsoidal rms axes $a > b > c$ from the inertia tensor I as follows, for instance for the minor axis c

$$c^2 = \langle z^2 \rangle = \frac{I_x + I_y - I_z}{2mN_i}$$

where the $\langle .. \rangle$ is the average of a quantity over N_i particles of mass m in the ith bin. From our simulations we recover spatially- and time-dependent axial ratios.

Figure 2 graphs the time-evolution of the axis-ratios b/a and c/a for four bins for the duration of an $N = 800,000$ run (d007 in Table 1). The configuration initially had a power index $\gamma = 3/2$. Since we start from spherical symmetry, both axial ratios are initially equal to 1. However, the rapid growth of radial motion leads to instability and the configuration quickly becomes triaxial (around $t = 5$ on the figure). Axial evolution slows down rapidly, until after $t \approx 20$ when the curves flatten out and begin to fluctuate about average values. What morphological evolution remains is largely confined to the innermost 20% mass bin, seen both for the minor c-axis and the median b-axis. Thus the inner region continues to evolve, albeit slowly, within the overall relaxed structure. A close look at Fig. 2 shows a gentle but steady increase of the minor-axis ratio c/a, from ≈ 0.38 to ≈ 0.43, for the innermost three mass bins of the system. The minor-axis ratio of the outer-most particles show no indication of evolution. By contrast, the ratio b/a evolves significantly for the 20% most bound particles only, from 0.58 to ≈ 0.65. This is suggestive of a trend toward axial symmetry as argued by Theis & Spurzem (1999) and Heller (1999) in their relaxation study of Plummer spheres (see also Curir & Diaferro 1994) . The example depicted on Fig. 2 suggests more rapid evolution in the inner, denser region of the system (shortest dynamical time-scale). We note that the initial conditions used here are without a harmonic (Plummer) core. The similar qualitative trends obtained from distinct sets of initial conditions supports the view that evolution toward axisymmetry is a generic feature of collision-less triaxial equilibria.
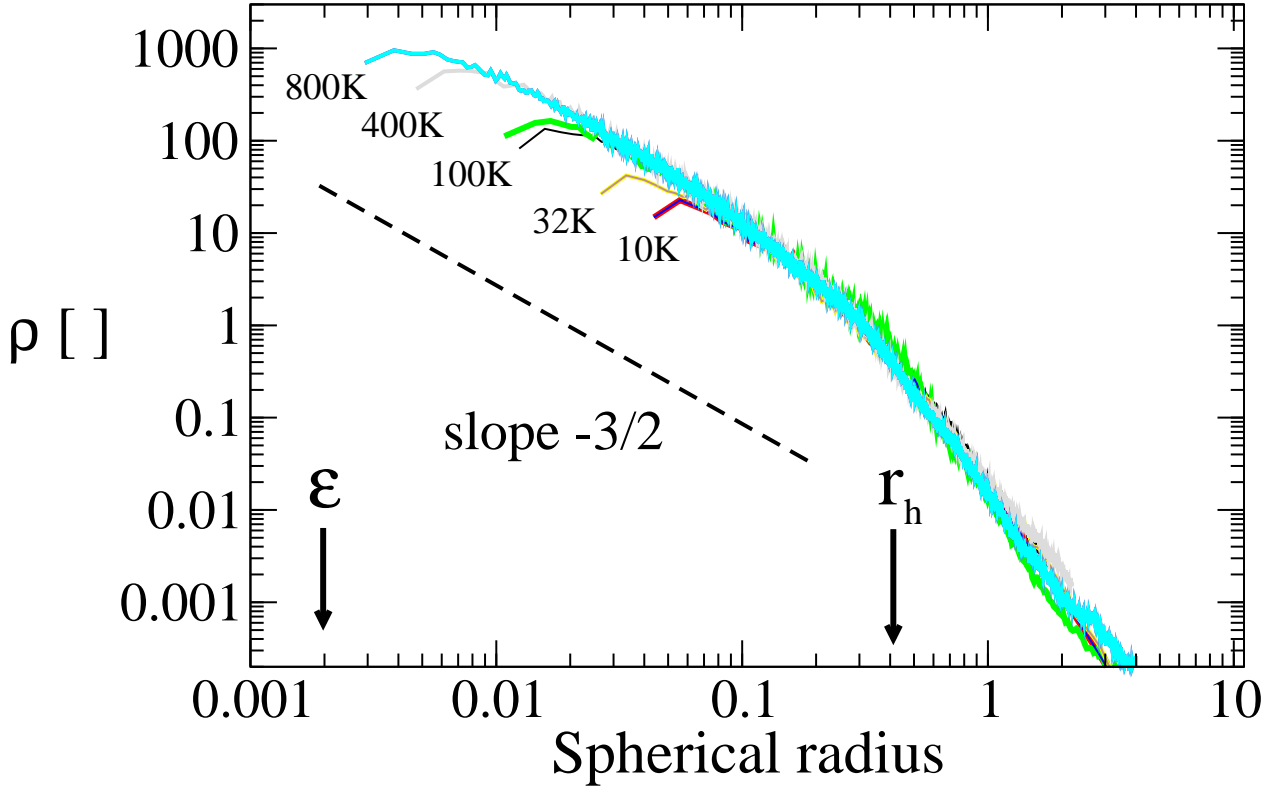
Figure 1. Density profiles of a series of runs with $\gamma = 3/2$. The number of particles for each case is indicated. The density was averaged over spherical shells containing 100 particles each, centered on the density maximum identified using the six-nearest neighbour scheme of Casertano & Hut (1985). The larger simulations allow deeper probing of the inner region. Two runs with $N = 100,000$ particles but different random number seeds are displayed to illustrate scatter. The smoothing length and half-mass radius are marked with arrows, and a straight line of slope -3/2 ($\rho \propto r^{-3/2}$) is shown for reference.
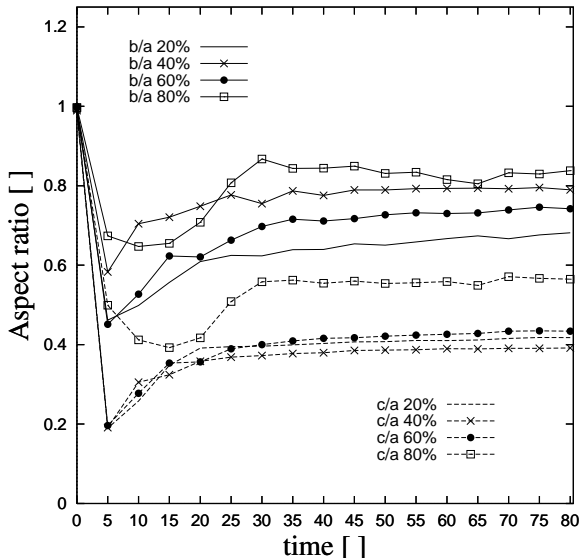
Figure 2. Time-evolution of the axis ratios for run d007.

## 4   Morphology of the equilibrium profiles

We now turn to a more quantitative inspection of our models. A&M+90 found from their 5,000-particle runs that the bulk of their triaxial equilibria shaped by the radial orbit instability are prolate (see their Table 1). This result was confirmed by C&H+92, who showed using 10,000-particle runs that the morphology of virialised objects varies in space, the equilibria being more triaxial prolate at the half-mass radius, and near-spherical in the inner and outer parts (see their Table 1 and Fig. 4). These studies set references against which to compare our results. In this section, we discuss the effect of varying numerical parameters (such as the number of particles and the softening) and model parameters (such as the index γ) on the equilibrium morphology; we consider parameterised fits to the density profiles in §5.

4.1   Quantifying morphology

A&M+90 introduced the parameter

$$\tau \equiv \frac{b-c}{a-c} \qquad (7)$$

to put the morphology of the relaxed equilibria on a quantitative footing. τ is bounded between 0 (prolate spheroids)
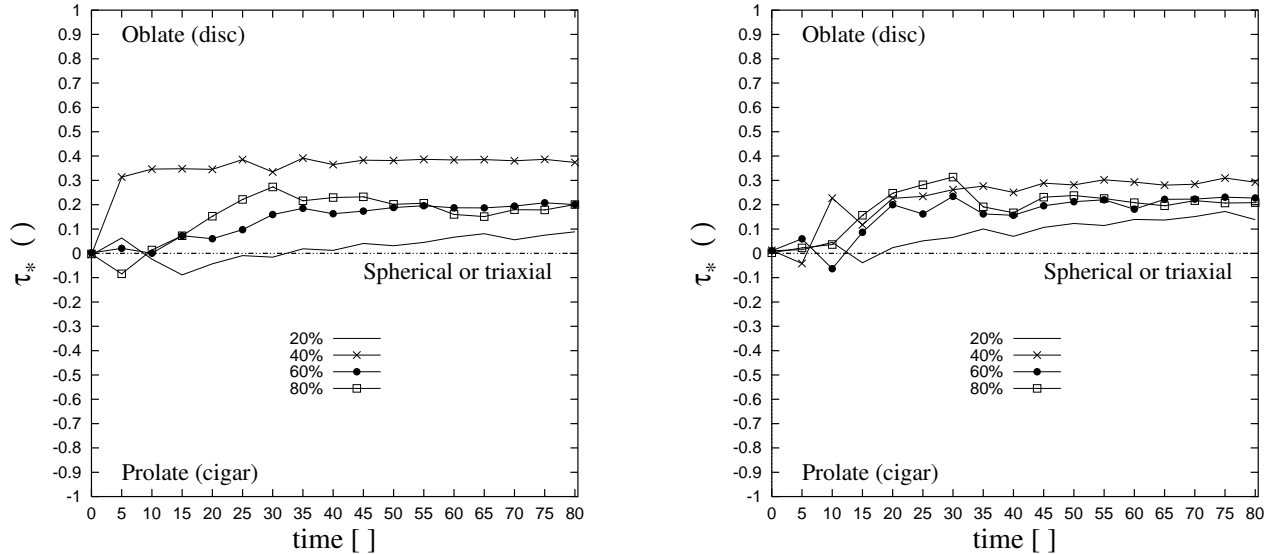
Figure 3. Time-evolution of runs d007 ($N = 800,000$ particles, left-hand panel) and d022 ($N = 200,000$ particles, right-hand panel). We graph the morphological parameter τ_* defined in (8) for different 20%-mass shells, as indicated.

and 1 (oblate spheroids). The degree of oblateness or prolateness varies within the bracket $[0, 1]$: configurations with $\tau > \frac{1}{2}$ are oblate, otherwise they are prolate.

In practice τ is sensitive to round-off errors when $a \approx b \approx c$. A clearer distinction between the three morphologies (triaxial, prolate and oblate) would be desirable. Consider instead the parameter

$$\tau_\star \equiv \frac{b^2 - c^2}{b^2 + c^2} - \frac{a^2 - b^2}{a^2 + b^2} \qquad (8)$$

which covers the range $[-1, 1]$; $\tau_\star = 0$ for a spherical distribution, while $\tau_\star > 0$ for 'oblate' triaxial distributions and < 0 for 'prolate' triaxial distributions. The parameters τ and $\tau_\star$ are related to each other and both increase monotonically with oblateness, however note that $\tau_\star$ allows to identify axisymmetric discs ($\tau_\star = 1$) or spindles ($\tau_\star = -1$) unambiguously. For this reason we have chosen to use $\tau_\star$ in our analysis.

As an example, the evolution of $\tau_\star$ with time is shown on Fig. 3, left-hand panel, for the $\gamma = 3/2$ case displayed on Fig. 2. Although on the whole the system achieves oblate morphology rapidly, the aspect ratios and hence the diagnostic $\tau_\star$ remain strong functions of the volume sampled. The innermost 20% mass shell first becomes mildly prolate before shifting to oblate shaped ($\tau_\star > 0$) after some 30 time units of evolution. This clearly serves as warning against hastily classifying the system globally as either prolate or oblate.

4.2   Dependence on N

We looked for trends in axis ratios $c/a, b/a$, and in $\tau_\star$ as function of the number of particles used in the calculations. Recall that relatively large variations are expected for $N < 10^5$ (BAK+02). To show that the results vary little whenever $N > 100,000$, first we graph on the right panel of Fig. 3 the

results of the same calculation as shown on the left but now with $N = 200,000$ particles. The trends and values over time of $\tau_\star$ are essentially the same as for the larger $N = 800,000$ calculation. This suggests that the numerics have converged for that range of values of N. However, full convergence has to be demonstrated through comparison with a set of results for smaller particle number.

We selected eight runs with N ranging from $N = 10,000$ to 800,000. Each run had a power-index $\gamma = 3/2$. To minimise root-N fluctuations we averaged aspect ratios over time from 60 to 80 (end of the calculations) for a total of 5 outputs. Table 2 lists their simulation parameters and aspect ratios and $\tau_\star$ achieved in equilibrium. (The aspect ratios were evaluated separately for four 20%-mass bins and for each output, however only values averaged over all mass bins are given.) We added to this compilation the results obtained by C&H+92 for this value of γ (their index n) and $N = 10,000$, as well as results from A&M+90, who considered cases with $\gamma = 1$ and $N = 5,000$. (A comparison of results from C&H+92 for the same $\gamma = 1$ values with those of A&M+90 shows a good agreement between these two studies.) The values of $\tau_\star$ computed from the data of A&M+90 were increased by $+0.15$ in account of the fact that they used a smaller γ and in anticipation of the trend seen in plots of $\tau_\star$ versus γ (see §4.4 and Fig. 6 below).

The results are graphed on Fig. 4, right-hand panel. We find predominantly oblate equilibria ($\tau_\star > 0$) for all our simulations with $N \geqslant 25,000$. Fig. 4 indicates less oblate structures from the $N = 10,000$ cases than for larger-N runs (open squares on the figure). We observe that the *full range* of axis ratios is reached only for $N \gtrsim 100,000$. Thus we find equilibria with ratios $a/c \approx 2.6$ for that order of particle number, well above the maximum $a/c \approx 2$ for 10,000-particle runs (cf. Fig.5, middle panels). The same conclusion applies to the major-to-median axes ratio.

The major- to minor-axis ratios of our 10,000 particle run, ranging from 1.6 to 2, all exceed those obtained by

C&H+92 for the same $\gamma = 3/2$ case. What is more, the results we obtained for τ_* differ significantly from those of both A&M+90 and C&H+92 (we get $\tau_* \approx -0.308$ from their Table 1): such results point systematically to prolate structures of equilibrium. Differences between our results and those of C&H+92 can not be attributed to particle number : below we make a detailed comparison of the initial conditions and software configurations to understand the origin of these differences.

4.3   Smoothing length issues

If ϵ is large we expect a loss of resolution and a bias in the outcome of the calculations. Burkert (1990) and Boily et al. (1999) have discussed this in terms of a cut off in orbit deflection angle from the mean field and artificial saturation of the phase-space density. We looked for such biases in a series of calculations with varying smoothing length.

Figures 4 and 5 (left-hand panels) graph the axis ratios and the averaged values of τ_* for the runs listed in Table 3. All runs had $N = 100,000$ particles. The averaging was done for the 80% most bound particles to facilitate comparisons with C&H+92. The error bar displayed (of 0.22, bottom-left panel) is scatter. The trend seen in the data clearly indicates that higher resolution runs yield more oblate structures. Note the apparent convergence achieved for $1/\epsilon = 256$, as τ_* and the axis ratios flatten out around that value.

The results of Fig. 4 and 5 underline the importance of using both sufficient number of particles and resolution for convergence of the equilibrium morphology. By contrast, the equilibria are not sensitive to the value chosen for the opening angle θ (Fig. 5, right-most panels). If we compare values of τ_* at $1/\epsilon = 10$ with those for $1/\epsilon = 512$, we find a systematic increase of $\approx +0.3$, enough to bridge the gap between our results for $N = 10,000$ particles and those of C&H+92 seen on the right-hand panel of Fig. 4. Thus, the reduced resolution of their calculation accounts for the most part for the strong prolate morphology of their equilibria.

4.4   Morphology in relation to γ

The sensitivity of equilibrium parameters to numerical resolution suggested to us to seek a relation between equilibrium morphology and initial density profile with higher-resolution calculations than was done in earlier work. On Fig. 6a we graph the ratio of major- to shortest-axis a/c as function of the power index γ. Table 4 lists the parameters of the $N = 100,000$ runs. The graph shows no trend with γ, with values of a/c (here averaged over the 80% most-bound particles) ranging between 1.4 and 2. On the figure we added the linear fit to the data from C&H+92 for the same quantity for comparison. The results of an $N = 10,000$ and an $N = 25,000$ calculation, with the same linear resolution $\epsilon = 1/512$, are also added in Fig. 6a. The 10,000-particle result falls close to the straight line from C&H+92, while the 25,000-particle run gives a ratio comparable to those obtained with 100,000-particle calculations. This confirms our expectation that 10,000-particle calculations do not quite reach maximum potential during violent relaxation (cf. BAK+02) and as a result do not achieve in equilibrium

the same final (converged) morphology of larger-N calculations. Note that the axis ratios for the cases $\gamma = 0$ and $\gamma = 2$ differ significantly from those obtained with other power indices. Nevertheless, the full range displayed on the y-axis of Fig. 6a brackets E2-E5 morphological types, which are by no means exceptional values when compared with those of elliptical galaxies.

On Fig. 6b we plot the values of τ_* as a function of initial power index γ. As before, the systems were split in equal 20%-mass shells to compute τ_* at times ranging from 60 to 80 N-body units. The scatter seen on Fig. 6b results form fluctuations between different mass bins. The solid line and filled symbols indicate averages. In contrast to the results for the aspect ratios, we find a well-defined trend of the parameter τ_* versus power index γ (Fig. 6b) such that τ_* increases on the mean with increasing γ, and $\tau_* > 0$ for $\gamma \geqslant 5/4$. The case with $\gamma = 2$ yields the most oblate and axisymmetric equilibrium of all the cases we have explored. Data points for $\gamma = 1$ and lower are only mildly oblate on the mean, while the case $\gamma = 1/2$ in fact gave a mildly prolate structure. However, the morphology of all runs with $\gamma \lesssim 3/4$ is consistent with axisymmetry or perfect-ellipsoid morphology ($\tau_* = 0$), owing to the scatter. Seen in this light, we would conclude that the morphology of systems with $\gamma \geqslant 3/2$ is oblate for all mass shells, whereas those with lower γ values are a mixture of oblate and prolate shells.

5   Global and inner density profiles

Fig. 1 displays typical spherically-averaged density profiles for our simulations with $\gamma = 3/2$. Our basic expectation from incomplete relaxation is that the density profile will match the power-law of the initial conditions on small scales. Power-law asymptotes at small and large radii are a generic feature of dissipation-less relaxation in cosmology (Navarro et al. 1997; Moore et al. 1998). It is natural to expect them also in the present, more restraint, context. We therefore set out to fit the radial density profiles of our equilibria with a continuous function of radius. All density profiles where averaged over spherical shells containing 100 particles. We varied the number of particles per shell (200, 500) but this did not lead to significant improvements, save for the very-large N d007 model where 500 particles still allowed to probe a sufficient range in radius while keeping the noise level low.

C&H+92 had found a good fit to their equilibrium $\gamma = 1$ run averaged over spherical shells using an Hernquist (1990) density distribution,

$$\rho(r) = \frac{M}{2\pi} \frac{r_0}{r} \frac{1}{(r_0 + r)^3}, \tag{9}$$

where M is the total system mass, and r_0 a free length. We also fitted the equilibrium profile obtained from an 100,000-particle $\gamma = 1$ run (d013, cf. Table 1) with (9). We first evaluated the density locally following the scheme of Casertano & Hut (1985) as coded in the NEMO analysis package. The rms axis ratios were found as in §3, again covering the innermost 80,000 particles only. This allowed us to round up the distribution, by shifting the particles in x-y-z *inversely* as the axial ratios obtained : thus the triaxial configuration
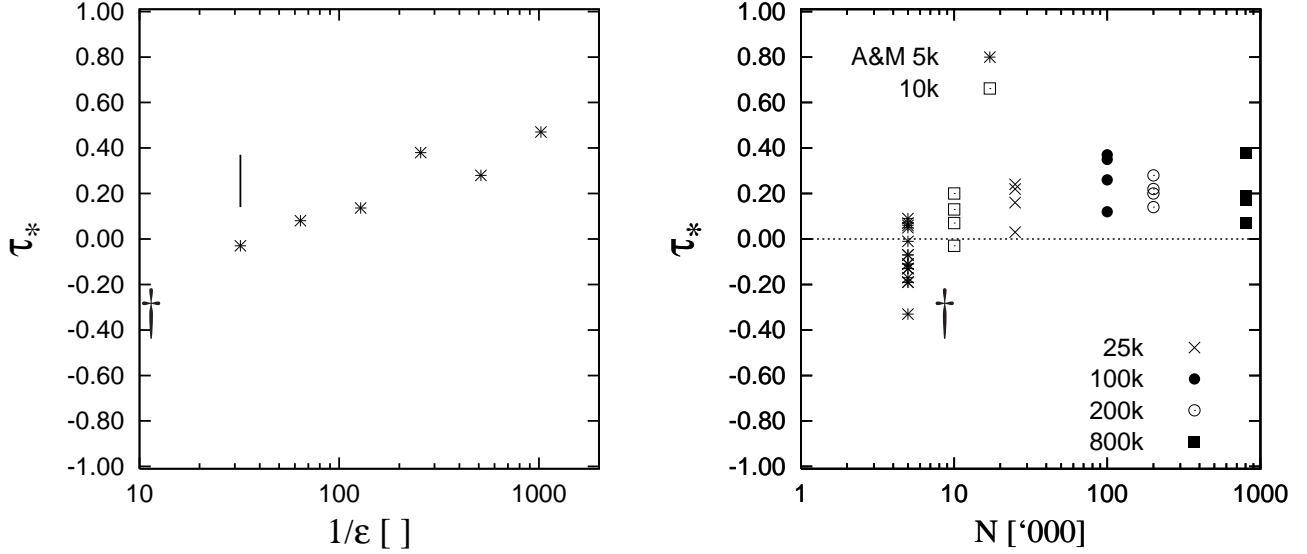
Figure 4. Global morphology parameter τ_* as function of inverse smoothing length $1/\epsilon$ (left-hand panel) and particle number N (right-hand panel). The vertical tick mark on the left panel is an error estimate derived from the scatter seen in the axial ratios; the data points are mean values for the innermost 80% mass. The data for the 5,000-particle runs are taken from A&M+90 but shifted upwards by +0.15 (see text for details). The symbol '†' is the mean value lifted from C&H+92 for $N = 10,000$.
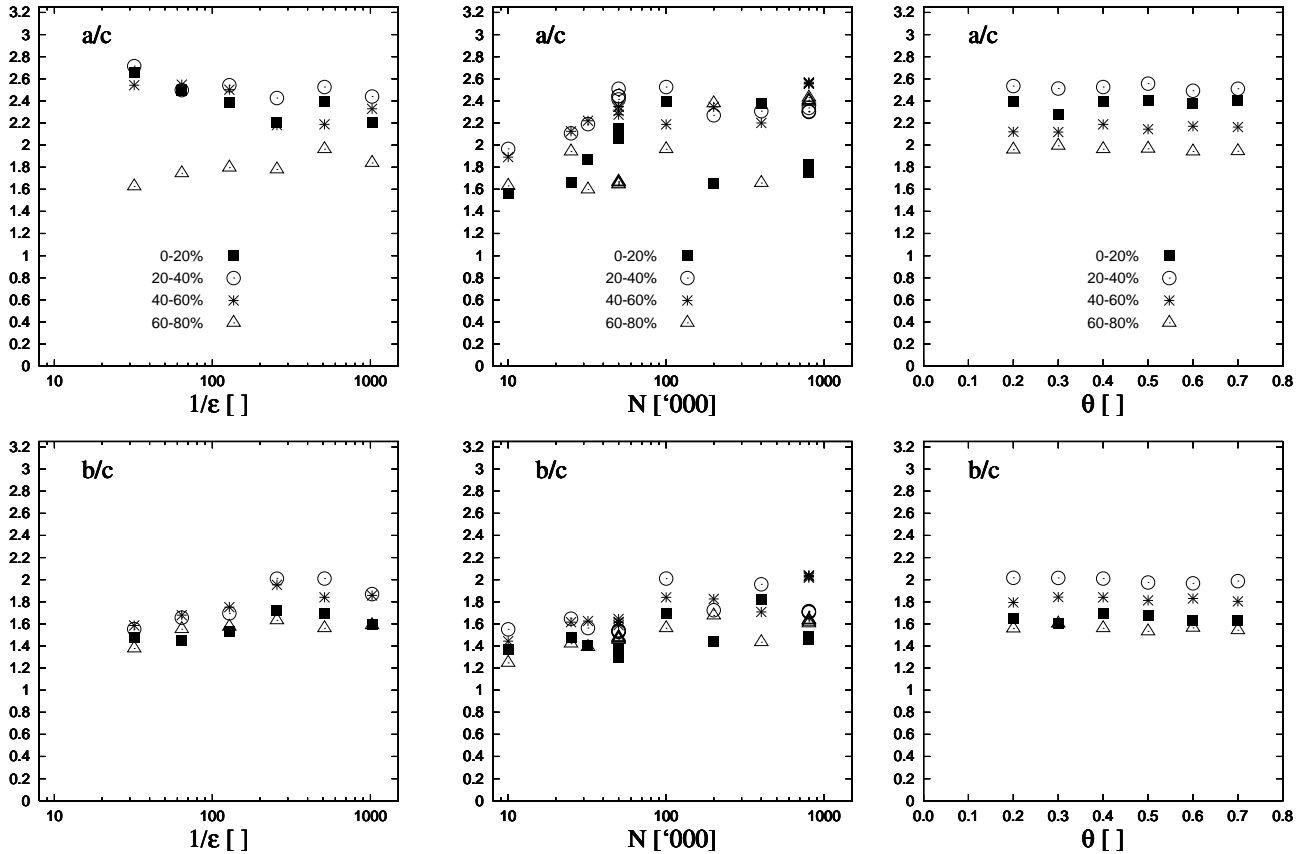
Figure 5. Axis ratios a/c and b/c as function of the opening angle θ (right-hand panels), particle number N (middle panels) and resolution $1/\epsilon$ (left-hand panels). Simulation parameters are listed in Tables 2 and 3. Values obtained for each of four 20% mass bins are displayed with different symbols.
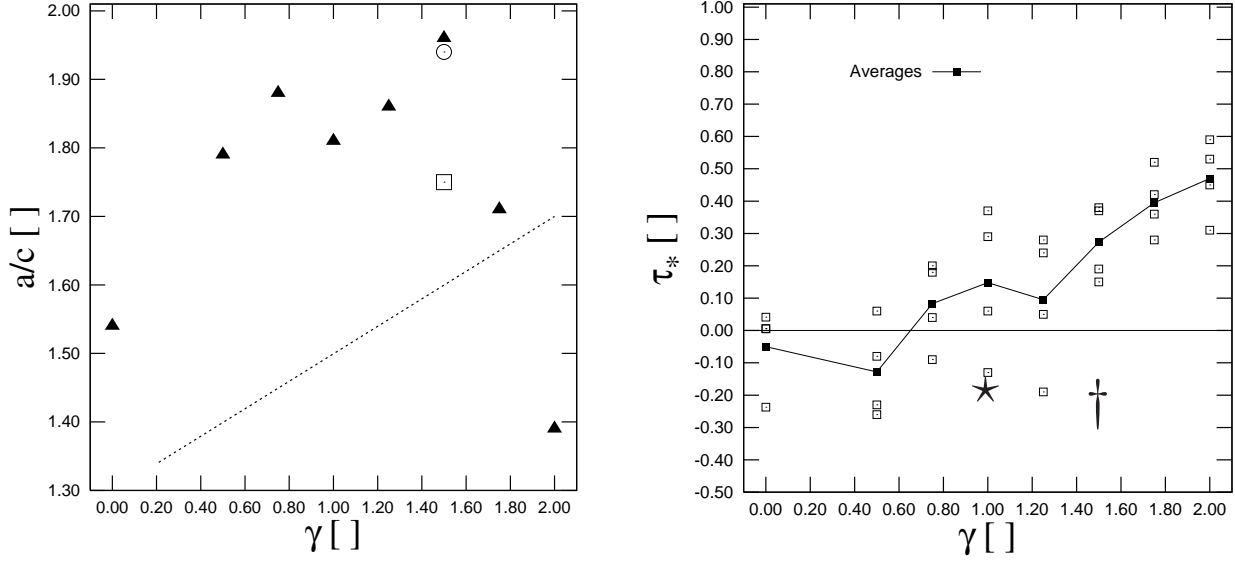
Figure 6. (A, left-hand panel) Ratio of major axis a to shortest axis c for runs with $N = 100,000$ particles (▲) and different power index γ. Results with 10,000 (□) and 25,000 (○) particles are also displayed for the case $\gamma = 3/2$. The straight dotted line is the fit $a/c = \gamma/5 + 1.3$ lifted from C&H+92. (B, right-hand panel) Shape parameter τ_* versus initial power index γ. The horizontal line indicates the boundary between oblate (positive) and prolate shapes. On the mean the structures are mostly oblate, more so for $\gamma > 1$. Averaged values for each γ are linked with solid lines. The star marks the average result of 5,000 particle $\gamma = 1$ runs from A&M+90; the dagger at $\gamma = 3/2$ marks the average result of 10,000-particle runs by C&H+92.
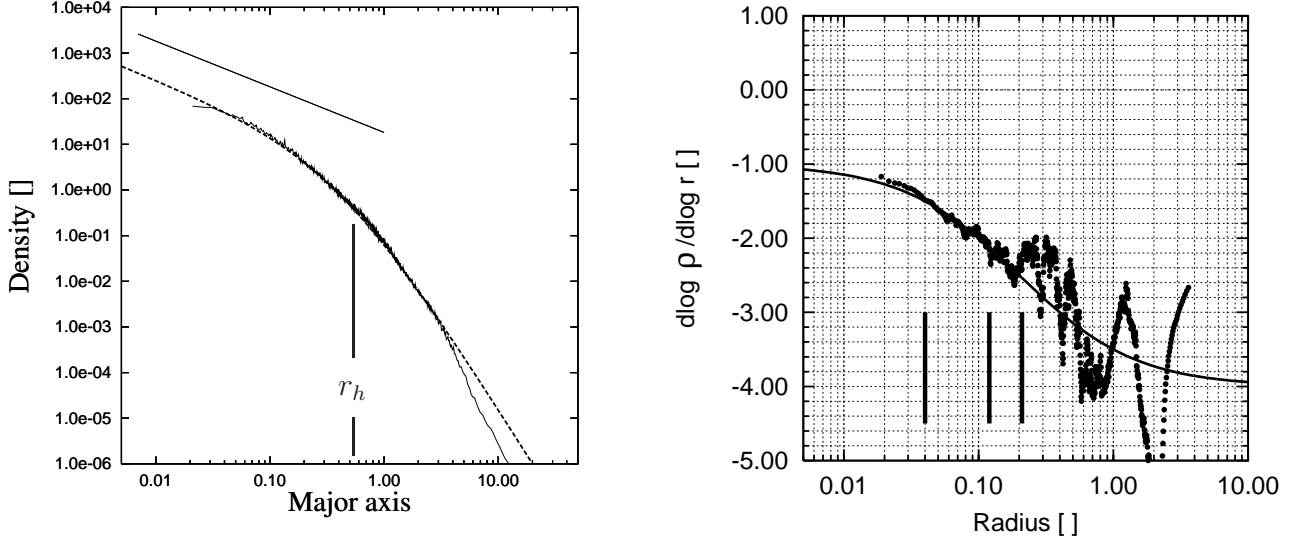

Figure 7. (A, left-hand panel) The equilibrium density profile of run d013 versus semi-major axis length. The dashed line is a fit of the data with an Hernquist model (Eq. 9). The straight line in the upper-left has a slope of -1 and the half mass radius r_h is given by a vertical tick mark. (B, right-hand panel) The logarithmic derivative of the density profile shown on panel (A). The solid line is obtained from Eq. 9. The vertical tick marks indicate (from left to right) the 1%, 10% and 20% most bound mass fraction.

was straightforwardly transformed to a sphere of the same volume.

The result is shown on Fig. 7a. The curve shown has $r_0 = 0.288$ with $M = 1$. Note that the half-mass radius ($r_h \simeq 0.53$) obtained numerically is significantly less than the Hernquist function $= (1 + \sqrt{2}) r_0 = 0.69(5)$ owing to

the mass deficit at large distance. Inside $r \simeq 10$ the mass integrated from (9) is 92.5% of the total, while the mass found numerically reaches 91.2% of the total. However, the data and analytic curve are in complete disagreement for $r > 10$. Nevertheless a comparison of this fit to the one shown on Fig. 8 of C&H+92 indicates that our larger-N
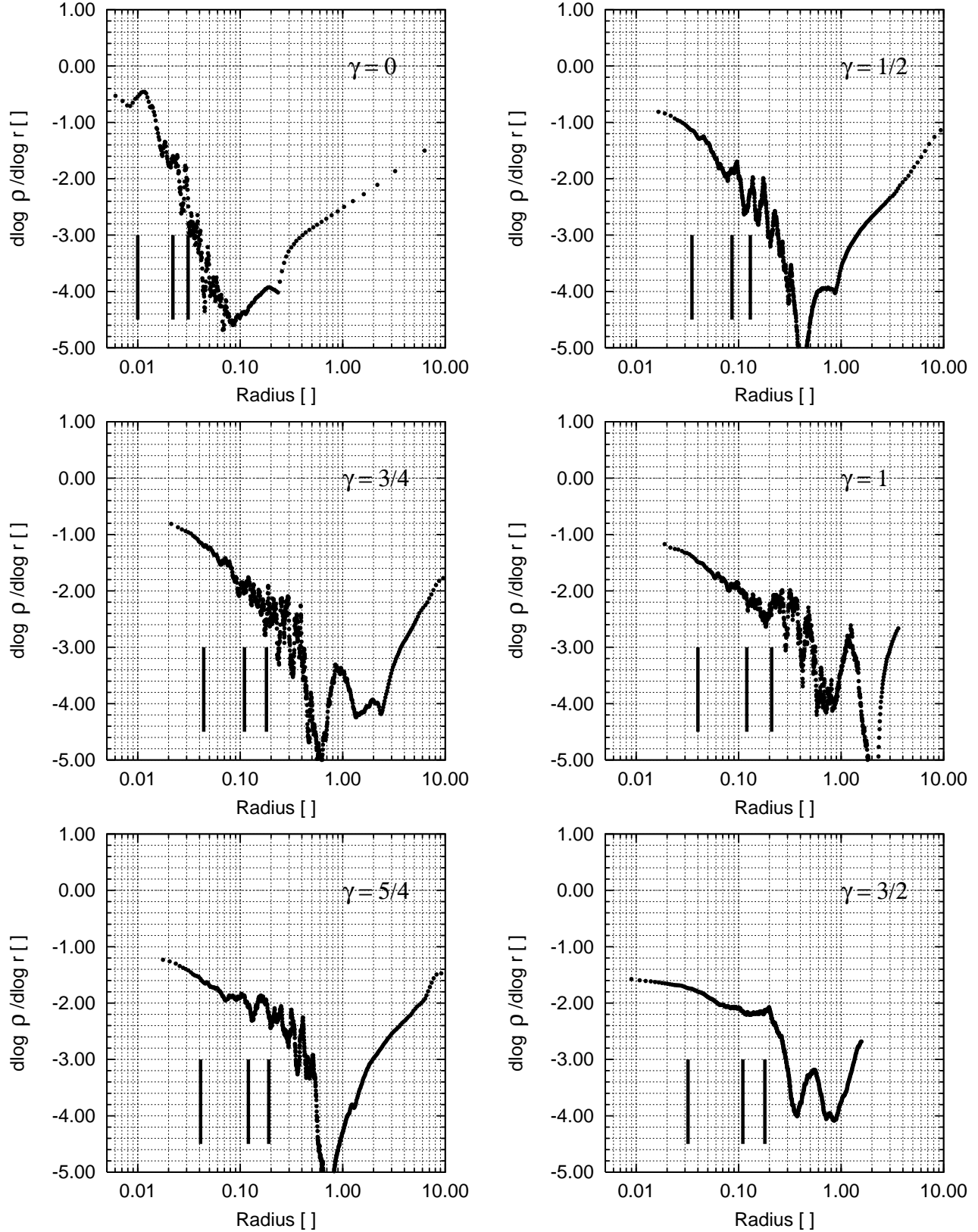
Figure 8. The logarithmic derivatives for equilibria obtained from different initial power-law index γ. $N = 100,000$ in all cases but for the case $\gamma = 3/2$ which had $N = 800,000$ particles. The vertical tick marks indicate (from left to right) the 1%, 10% and 20% most bound mass fraction.
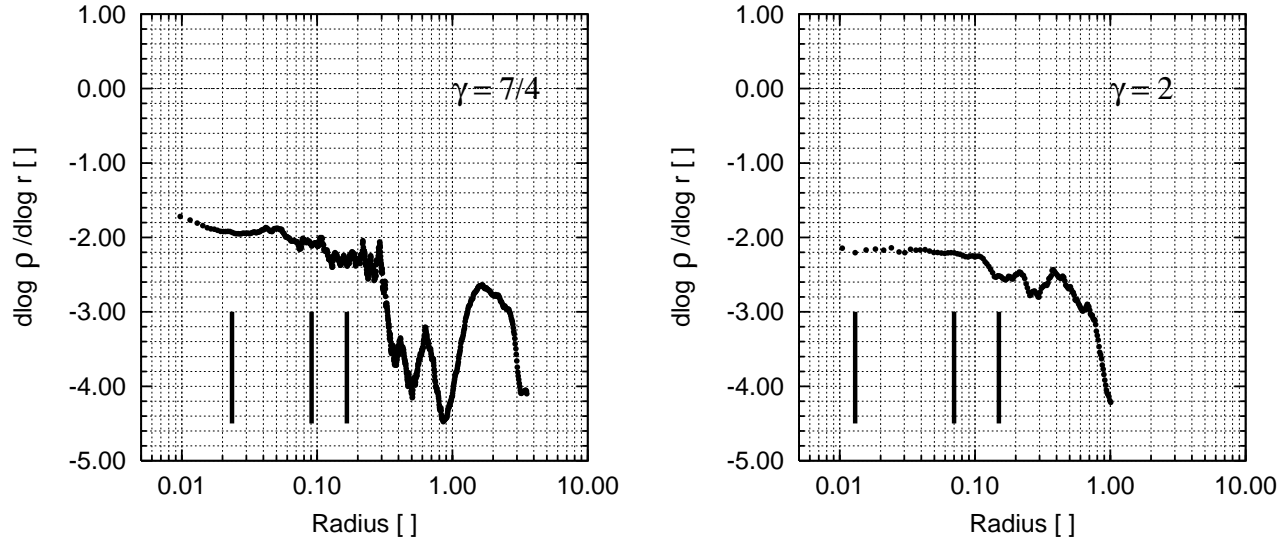
Figure 8. – *continued*

simulations give an ever closer agreement to the Hernquist profile. The fact that both profiles are relatively well fitted by the Hernquist law is unexpected, since the morphology of the two equilibria are very different from each other (oblate here, cf. Fig. 6b, and prolate in C&H+92).

5.1   Logarithmic derivative : $\gamma = 1$

One reason why a global function does a poor job of fitting the mass distribution is the irregular, noisy profiling outside (about) the half-mass radius. We illustrate this with a series of graphs of the logarithmic derivative of the density as function of radius. A piecewise linear fit to the finite-difference scheme was done, such that

$$\left.\frac{d\log\rho(r)}{d\log r}\right|_i = \frac{\log(\rho_i/\rho_{i+k})}{\log(r_i/r_{i+k})} \qquad (10)$$

where $i := [1, 1000 - k]$ is the index of a mass shell, and $k \approx 30$ is constant. The value of k is chosen so as to sample a sufficiently large radial increment and avoid round-off errors in (10). We found that k could be increased to ≈ 200 without affecting the overall picture much. We then used a least-square fitting routine (Press et al. 1992) to find the best linear fit over k points. The result was centered on the mean radius in the interval $i, i + k$.

On Fig. 7b we graph this derivative for the run $\gamma = 1$ listed in Table 4. We have indicated the radii of the inner 1%, 10% and 20% mass shells with vertical ticks on the figure. It is clear that the derivative is smooth and well fitted up to the 20% mass shell; however beyond that point large fluctuations are seen which indicate grainy or irregular substructures. Note also that the data match very well the logarithmic derivative of (9), given by a solid line on the figure, from the innermost 0.1% mass bin up to roughly the 20% mass radius. Note the apparent clustering around $d\log\rho/d\log r \approx -2.2$ also between the 20% and half-mass shells ($r_h \simeq 0.53$).

Beyond the half-mass radius the derivative oscillates wildly between values of -3 and -4; beyond $r = 1$ or so the data is more erratic.

5.2   Logarithmic derivative for all $\gamma's$

It may come as a disappointment that the logarithmic derivative on Fig. 7b has not converged to the anticipated constant value $= -1$, despite the very small innermost mass fraction (0.1%) sampled. We asked whether the same was true of all the runs with different γ's. We therefore repeated the procedure for all runs listed in Table 4, except for the case of $\gamma = 3/2$ where we took the results from the 800,000 particle run. The results are displayed on Fig. 8. Here again the vertical ticks indicate 1%, 10% and 20% mass shells. For small values of γ, $d\log\rho/d\log r$ does not converge to a flat value as we approach the center. However, as we consider larger values of γ we find hints of such a convergence, particularly for $\gamma \geqslant 3/2$. Once more we find a suggestion of a leveling off around $d\log\rho/d\log r \approx -2.2$ at radii close to the 20% mass shell for all the cases with $\gamma \geqslant 1$. In their treatment of the Boltzmann equation in one dimension, Hozumi et al. (2000) also found a power-law fit of index ≈ -2.1 around the half-mass radius of their systems.

5.3   Circular velocity

On Fig. 9 we graph the (less noisy) circular velocity $v_c = \sqrt{GM/r}$ as function of the radius and of the integrated mass. Note that $v_c \to$ constant when $\rho(r) \propto r^{-2}$. On the figure we also added a straight line ($\propto r$ or $\propto M^{1/3}$) that v_c would follow if the density flattened out at the centre. For our simulations, v_c rises slowly as a function of radius and we find $v_c \approx r^{0.75}$ gives a rough fit for runs with $\gamma < 1$. Starting with the curve $\gamma = 1$, one can see a plateau appearing at a mass fraction $M(< r)/M \approx 0.1$, which becomes more prominent for increasing γ. The circular
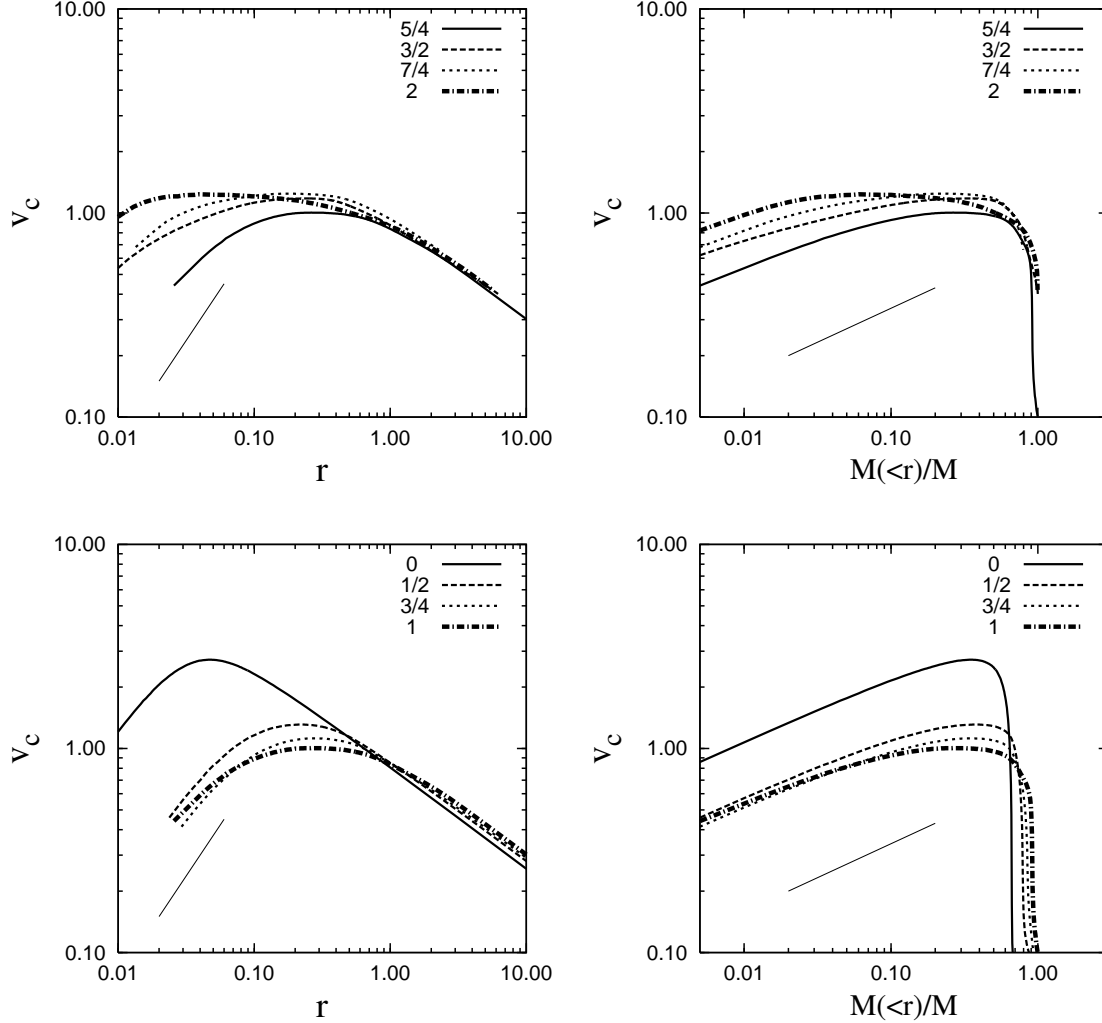
Figure 9. Rotational velocity v_c plotted for different γ as function of radius (left-hand panels) and of integrated mass $M(< r)$ (right-hand panels). Lower set : $0 < \gamma \leqslant 1$. Higher set : $1 < \gamma \leqslant 2$. The straight lines are $\propto r$ (left-hand panels) or $\propto M^{1/3}$ (right-hand panels) corresponding to a constant mass density.

velocity drops off in a Keplerian tail at large radii, in all the cases. We remark that the maximum of v_c nearly always occurs at the mass fraction $M(< r)/M \approx 1/3$ while the maximum itself is a non-monotonic but nearly flat function of γ (save $\gamma = 0$, see Fig. 10). Therefore, while none of the equilibria can be mapped into another (different rotation curves, mass profiles), the results of collapse calculations for different γ's (and hence the accretion rates or history) are fairly similar in terms of $\max(v_c)$, and of corresponding mass fraction and radius, a situation that parallels current debates about the universality of resolved circular velocities and virial masses in cosmology (see e.g. Power et al. 2003; Navarro et al. 2004). Only the two cases of $\gamma = 0$ and 2 stand out. These cases are particularly interesting, since they produce the largest and second largest maximum v_c, but the smallest corresponding radius and mass fraction (bottom panel, Fig. 10).

5.4 Power-law limit

The search for a flat logarithmic derivative can be done through a functional fit which admits a linear regime in $\log r$. We modified (2) slightly to look for fits to the derivatives of the form

$$j(r) \equiv \frac{d \log \rho}{d \log r} = -\gamma_f - \gamma_2 \log r - \beta \frac{r^2}{r^2 + r_o^2} \qquad (11)$$

where r_0 and β are as before, the symbol γ_f is used to distinguish the final and initial values of γ and the constant γ_2 is equal to the second derivative at small radii to $O(r^2)$. We imposed $\beta = 4 - \gamma_f$ so three parameters remain free. A strict power-law at short distances must yield $\gamma_2 = 0$. We applied the functional $j(r)$ to three cases with $\gamma = 3/2, 7/4$ and 2. The results are shown on Fig. 11. The data points are those of Fig. 8 in each case, to which we have added $j(r)$ (solid line) and $j'(r) = dj(r)/d \log r$ (dashed line). We find $j'(r) < 0$ everywhere for $\gamma = 3/2$, however a fit with $\gamma_2 = 0$ gave sensible results for both $\gamma = 7/4$ and 2. Even
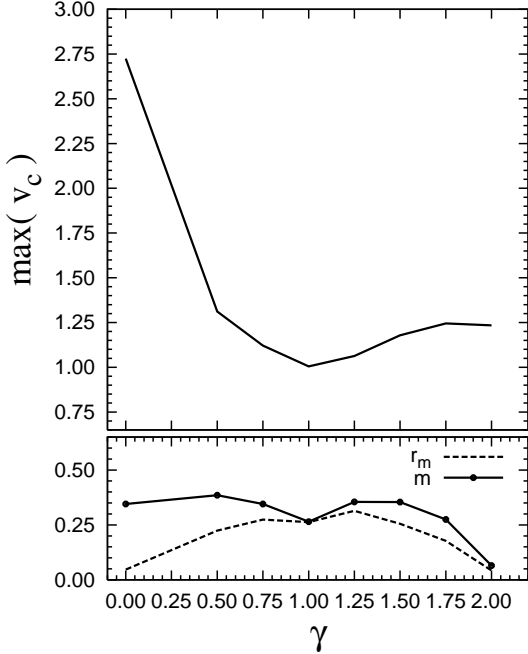
Figure 10. Maximum of the circular velocity v_c as function of the initial power-index γ (top panel). The lower panel shows the mass fraction (m) and radius (r_m) at maximum.

so the power-law regime in the case $\gamma = 7/4$ does not cover more than a few percent of the system mass, while it extends roughly out to 10% of the mass for $\gamma = 2$.

Although the anticipated relation $\gamma_f = \lim_{r \to 0} -d \log \rho / d \log r \approx \gamma = $ constant at small radii is not recovered, a strong correlation is found between γ and the minimum of $-d \log \rho / d \log r$ read off Fig. 8. We graph $-d \log \rho / d \log r$ for the innermost 1% (solid) and 0.1% (dotted) mass shells on Fig. 13. The diagonal on that figure is the sought equality $\gamma_f = \gamma$. We find a clear trend, especially for $\gamma \geqslant 3/2$, the strongest for the innermost 0.1% of the mass. For runs with $\gamma < 1$ the correlation is more suggestive, even for the innermost 0.1% mass shell.

As long as we are concerned with the radial profile of the systems at small r, these results show that memory of the initial configuration, while still there, involves only a very small fraction of the total mass. Correlations in binding energy have been noted by several authors (see e.g. van Albada 1982; Henriksen & Widrow 1999), so the initially most-bound particles are those contributing to correlations seen on Fig. 13. We deduce that well-resolved equilibria could not have inner cusps with a logarithmic slope lower than γ of the initial conditions. But significant deviations already at the 1% mass fraction means that this conclusion effectively applies to a very small volume. We may ask whether the velocity field also shows traces of the collapse, and in what measure.

6   Phase-mixing and relaxation

6.1   Cold initial conditions

Having brought to light a trend for the run of density in equilibrium as function of the initial power index γ (Fig. 13), we

now ask whether a similar relation exists for the velocity field. Repeated exchanges of kinetic energy modify a particle's velocity by $\delta \boldsymbol{v}$ (say) each time. When these boosts in velocity are randomly oriented the ensuing velocity vector is uncorrelated with the initial $\boldsymbol{v}$. This will be true in an average sense when the sum of all perturbations exceeds the norm of the velocity vector, i.e. $\sum_i \delta \boldsymbol{v}_i^2 > \boldsymbol{v}^2$. For systems collapsing from rest, $\boldsymbol{v} = 0$, this condition will be met first by particles that do not acquire large velocities while the background potential changes rapidly. From these considerations, we would expect the velocity field to be the one arising from violent relaxation for all orbits with relatively small in-fall velocities. Because of the enforced spherical symmetry of the initial conditions, all orbits are radial ($\boldsymbol{v} = v_r \hat{\boldsymbol{r}}$) at the on-set of collapse. The work by the gravitational force $\delta v_r^2 \propto r \nabla_r \phi \propto r^{2-\gamma} \to 0$ for all γ's < 2. The kinetic energy remains small for all particles orbiting near the centre and hence small fluctuations in energy will wipe out memory of the coherent radial collapse.

A Maxwellian coarse-grained velocity distribution function (d.f.) (more precisely: a sum of Maxwellians) is the signature of violent relaxation, a fully stochastic redistribution of kinetic energy. Merral & Henriksen (2003) and Iguchi et al. (2005) have obtained good agreement with this prediction by integrating the collisions-less Boltzmann equation directly, and evaluating the velocity d.f. $f(v)$ in equilibrium at the origin of the coordinates. The same procedure can not be done here due to finite resolution. Instead, we evaluated $f(v)$ for an 100,000-particle $\gamma = 3/2$ calculation by sorting and binning in velocity space all particles within a given mass fraction. We picked a fraction $M(<r)/M = 2.5\%$ which samples the regime where the logarithmic derivative is (roughly) linear with the logarithm of the radius, that is, the density $\rho \propto r^{k \ln r}$ with k some numerical constant (cf. Fig.8) and much larger than the softening length $\epsilon \simeq 0.002$. For comparison, we also computed $f(v)$ for all particles, taking care to normalise the d.f. so that it integrates to unity in each case.

The results are displayed on Fig.12. We find excellent agreement with a Maxwellian profile for the inner 2.5% mass sample despite the rough dataset used (2,500 particles only)[3]. Applied to the system as a whole, we find an overabundance of low-velocity particles, while overall the fit is not as good (see Fig. 12, right-hand panel). The excess probability density at low-velocities with respect to an isotropic Maxwellian velocity d.f. may be understood as an overabundance of stars on low-energy radial orbits. Stars on such orbits spend more time at apogalacticon, where their velocity is relatively low. This is confirmed by looking at runs of the isotropy parameter $\beta_* \equiv 1 - 1/2 \langle \sigma_\perp^2 / \sigma_r^2 \rangle$ distinguishing between perpendicular ($\perp$) and radial velocity components (top panels, Fig. 12). Clearly $\beta_* = 0$ for an isotropic velocity field, and $\beta_* > 0$ when the system shows an excess of radial motion. We find the inner region more nearly isotropic (left-hand set), while globally β_* assumes larger values and increases as v^2 decreases (right-hand set).

In conclusion, we find a good fit to the inner region

---

[3] A repeat with the 800,000-particle run, or by averaging over time intervals $\gg$ the local dynamical time, only confirms the quality of the agreement.
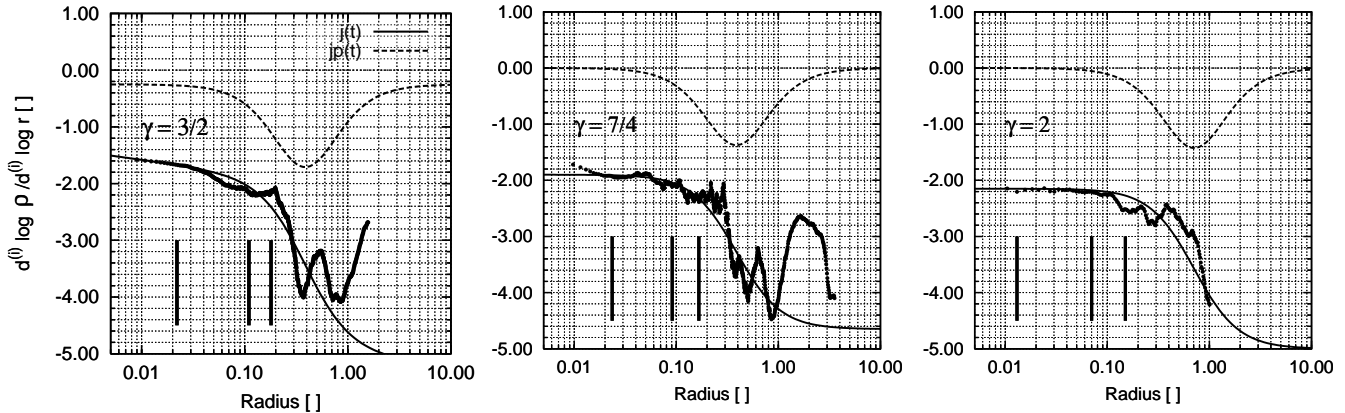
Figure 11. Logarithmic first and second derivatives versus radius for the three cases with the largest initial power index γ. The solid line is a fit (j) and the dashed line the derivative of that fit (j', top-most curve). A strict power-law is ruled out in the case $\gamma = 3/2$ everywhere. For $\gamma = 7/4$ a power-law inner profile out to $\approx$ a few percent of the mass is representative; while for $\gamma = 2$ the constant power-law region reaches $\approx 10\%$ of the total mass.

velocity d.f. with a Maxwellian, while globally this does not hold. These results go in the same directions as the findings by others (e.g., Funato et al. 1992; Merrall & Henriksen 2003; see also Bertin & Trenti 2003) but for fully three-dimensional calculations. By the time particles fall in with large velocities, much orbit crossing (and therefore phase mixing) has gone on in the centre. As a result, the potential varies more smoothly in time and these particles preserve significant radial motion. This is seen in animated snapshots, when the last mass shell has collapsed and particles rebound from the central region. A fraction of them are unbound and leave the system.

6.2 Warm initial conditions

We wish to assess how equilibrium profiles of simulations with $Q \neq 0$ initially differ from those starting from rest. Since kinetic energy provides pressure support, a run with $Q > 0$ will collapse more slowly (reduced mass in-fall, $\dot{m}(t)$). The expectation drawn from simulations with different γ's is that a reduced rate of in-fall (large γ, cf. Eq. 6) would favour oblate morphology in equilibrium (cf. Fig. 6b). A&M+90 have shown that sufficiently warm collapse simulations shut off ROI's and preserve the symmetry of the initial configuration. (The limiting case of an initial $Q = 1$ equilibrium must trivially preserve spherical symmetry.) The question at stake here is whether ROI modes of instability are washed out progressively as Q increases from zero, leading to more and more spherically symmetric equilibria; or whether more oblate equilibria first develop for $Q > 0$ but small, before being washed out.

In order to answer this question we ran a series of simulations with warm initial conditions. We set up Dehnen (1993) density profiles, Eq. (2), with $\gamma = 3/2, \beta = 5/2$, $r_0 = 0.756..$, which are truncated at radius $r_t \approx 3.76$ so that the density profiles of these models match the density of the power-law models at the centre. This choice of scales allowed us to use the same numerical setup (smoothing length and time-steps) as for the power-law computations since the dynamics at the centre is identical in both cases. The to-
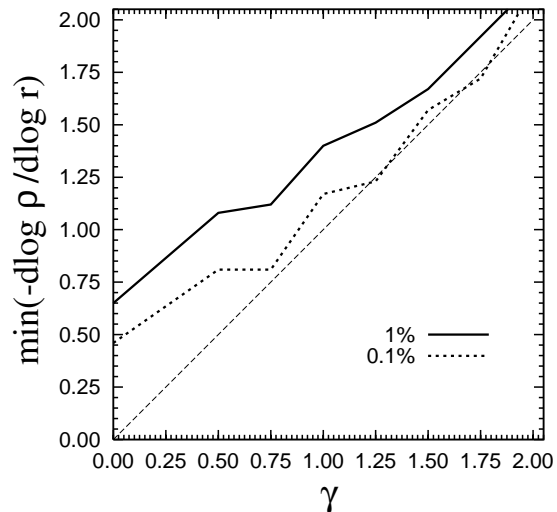

Figure 13. Value of the logarithmic derivative $-d\log\rho/d\log r$ as function of the initial conditions power index γ for two mass shells of 1% (solid line) and 0.1% (dash). The latter is the minimum positive value obtained for each case. The diagonal broken line is equality.

tal mass $M(< r_t) = 1$ as before. As explained in §2, we attributed velocities according to an isotropic Maxwellian velocity d.f. constrained to satisfy locally the first moments of the Jeans equations (Binney & Tremaine 1987). The outcome of such studies are not sensitive to details of the velocity field but to the global value of Q (Barnes et al. 1986; A&M+90).

6.2.1 Similarity patterns

A self-gravitating collapse proceeding from power-law initial conditions soon develops single-valued orbital patterns, such that any star follows the same orbit as any other once the scales of mass and lengths are renormalised un-
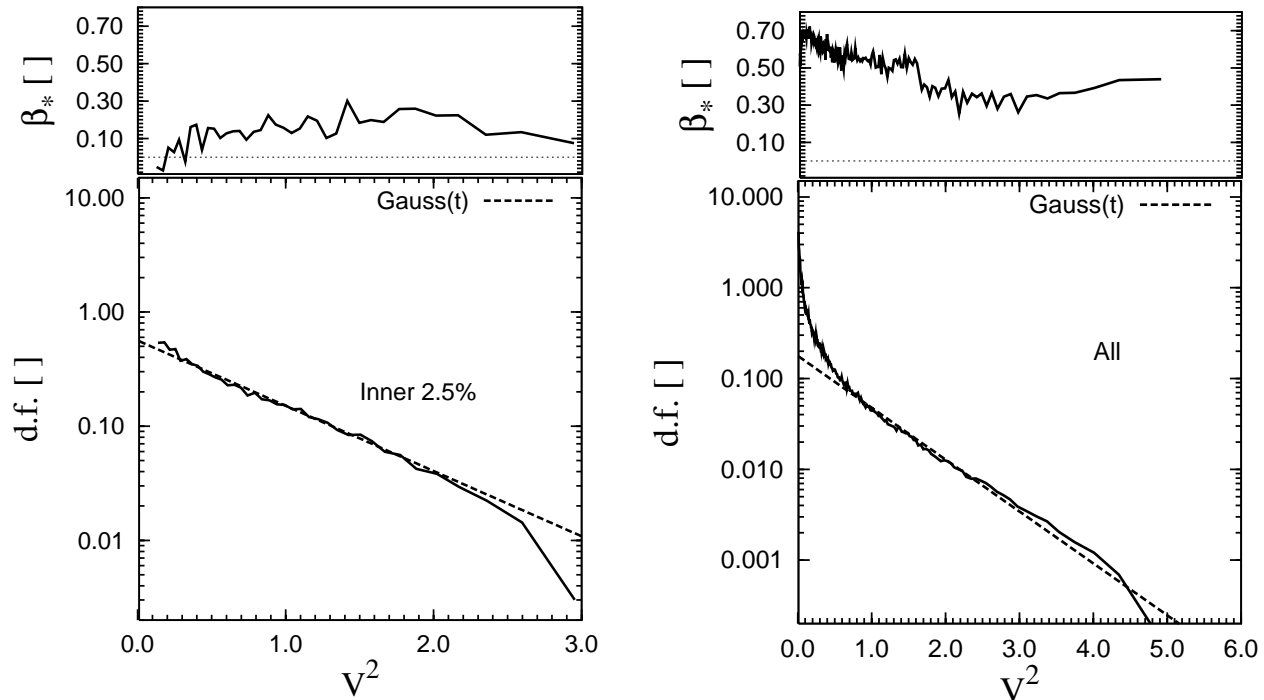
Figure 12. The velocity d.f. $f(v)$ as function of v^2. Note the logarithmic scale. The function was constructed for the innermost 2.5% particles at the end of the simulation (left-hand panel). The same quantity computed for the system as a whole is shown for comparison (right-hand panel). The dashed curve is the same Maxwellian on both panels; the axes were rescaled for better display. The top panels show runs of the anisotropy parameter $\beta_* \equiv 1 - 0.5 \langle \sigma_\perp^2 / \sigma_r^2 \rangle$; $\beta_* > 0$ for systems with excess radial motion. The inner part (left-hand set) is more isotropic, while globally the system shows an increasingly anisotropic velocity field as we reach the edge of the system ($v^2 \to 0$).

der a time-transformation. The trajectories of the stars map out a unique path and the flow is said to be self-similar. The growth of similarity patterns saturates to give way to a phase-mixing instability leading to virialised equilibrium (Henriksen & Widrow 1997, 1999). An example of this process is displayed on Fig. 14, which compares the run of the radial velocity with radius for two time sequences, one corresponding to a cold collapse (d002) and the other to a warm one (h002). From this, and other similar plots for other simulations and other times (not shown here), it is clear that the self-similar pattern remains well defined for a longer time in the warm run than in the cold one. This is in good agreement with Merral & Henriksen (2003), who argued that warm initial conditions slow down the transition to a phase-mixing instability. This trend, however, is not monotonic. Indeed, for very hot runs, such similarity patterns hardly show up. Thus, intermediate values of Q, of the order of 0.1 or 0.2, are the optimum for their formation and maintenance.

We also note that, for the warm simulation, the radial velocity dispersion is relatively large at the earliest time, and for sufficiently high Q values some particles even have $v_r > 0$ and outward motion. As time runs, the radial flow becomes cooler (the one-stream at large radii becomes thinner). In the late stages the one-stream in-falling material is more and more fine-tuned (single-valued), as in the cold collapse. This observation will serve us below when interpreting the structural evolution of the models during collapse.

6.2.2 Oblate, and then not

Table 5 lists the overall morphology in equilibrium of a series of Dehnen models with $\gamma = 3/2$ and different Q initially. The total runtime was 80 time units in each case. All collapses with $Q > 0.4$ (not listed in Table 5) led to highly spherical equilibria. For $Q \leqslant 0.4$ we get either prolate or oblate morphologies. For the coldest cases ($Q \leqslant 0.05$) the equilibria are oblate, as the scale-free models. With increasing Q, the equilibria first shift to prolate and then to spherical symmetry. This is rather different from the monotonic trend we would have anticipated, had the aspherical modes of instability been washed out progressively with increasing Q. The transition is very sharp around $Q \approx 1/10$. Two possible explanations of this phenomenon are on hand. The first invokes the growth of a bending-mode of instability, similarly to self-gravitating thin discs (see Merritt 1999). Here, the highly elongated prolate morphology of the cold (low Q's) runs implies motion mainly down the semi-major axis. As Q is reduced and the bar achieves a highly prolate shape, an off-axis mode of instability will develop owing to the large velocities of the particles parallel to the semi-major axis. Comparing centrifugal and restoring forces in the case of a thin bar distorted by a sinusoidal bend of wave-number $\kappa = 2\pi/\lambda$ and amplitude $\mathcal{A}$ immediately gives the condition $\mathcal{A}\kappa >$ constant for growth of the mode (the precise value of the constant is of no interest here). A similar relation applies for discs. Clumping modes of short wavelengths (large κ) will develop more easily in cooler systems, whence the observed

Figure 14. Phase-space sections showing the radial velocity as function of radius during in-fall for two runs, one starting from zero velocities (d002, left-hand set) and the other from sub-virial velocities (h002, right-hand set). A similarity pattern shows up in the form of concentric rings, which are progressively deleted at later times.

transition to oblate morphology. An alternative explanation is that a two-stream mode of instability develops more fully in the deep potential well of the colder collapses, when the in-falling material reaches larger velocities and more orbit-crossing takes place at the centre. Clearly a stability analysis well into the non-linear regime is required to determine which one of the two (or other) types of instability prevails. Such an analysis goes far beyond the objectives of the present paper and will not be attempted here. The close link between equilibrium properties and initial virial ratio was noted long ago for spherically averaged values (van Albada 1982; Mclynn 1984; A&M+90), however, to the best of our knowledge, the transition from oblate to prolate morphology and then to spherical symmetry as Q increases has not been stressed before.

We close this section with a comparison of the cold $Q = 0$ collapse from a power-law profile with the corresponding Dehnen model. The cold Dehnen run listed in Ta-

ble 5 reached $\tau_* \approx 0.4$ in equilibrium, i.e. more oblate than what was obtained from an $\gamma = 3/2$ power-law initial conditions (cf. Fig. 4 and Table 4). Since the mass profile of a Dehnen model is steeper at large radii than $\rho \propto r^{-3/2}$, mass shells falling in from large r take longer to reach the origin in that case. In other words, the rate of mass in-fall of the Dehnen sphere is lower compared to the case of collapse from a power-law profile. This further supports our claim that a reduced rate of mass in-fall $\dot{m}$ (cf. Eq. 6) leads to more oblate equilibria, at least when the initial virial ratio $Q = 0$.

7   Summary and discussion

Using N-body computer simulations, we have shown that collapsing self-gravitating spheres develop oblate or prolate triaxial figures of equilibrium. In a study of numerical convergence, we have shown that an insufficient number of particles N, or linear resolution ϵ, can give wrong results for the

morphology. As N increases we find evidence for a slow drift from prolate to oblate morphology; the trend is similar but more pronounced when we *reduce* the smoothing length ϵ. Previous studies had found prominently prolate structures of equilibrium, but this appears to have been due partly to the numerical setup used. The degree of symmetry of the virialised structures is highly sensitive to the phase-mixing which takes place during in-fall. We used scale-free power-law initial density profiles and found that steeper powers lead to more oblate equilibria. We also noted that increasing the initial virial ratio $Q > 0$ leads to prolate equilibria. Increasing Q to yet larger values has the effect of maintaining spherical symmetry, by shutting down aspherical modes of instability (Barnes et al. 1986). For very low-Q calculations, we noted that the prolate equilibria give way to oblate shape and have invoked two mechanisms that likely play a role in this transition (§6.2). A full analysis of that phenomenon is deferred to a future study.

All our simulations lead to peaked central regions. When fitting the run of spherically-averaged volume density with radius we found that the logarithmic derivative of the profiles converges only slowly to a power-law, at least when $\gamma \leqslant 3/2$ (Fig. 8). The logarithmic derivative in the central region of the equilibrium systems is well correlated with γ when $\gamma \geqslant 3/2$ (Fig. 13); in all cases, the central cusps would include only a very small fraction of the total mass, on a scale where the impact of baryonic (i.e., gas) physics would not be negligible. Collisional relaxation effects are always a worry in dense central regions. We checked that the collisional time of our simulations is too long, even at the centre, for two-body encounters to play a role. Power et al. (2003) conducted a thorough analysis of these effects. We find our simulations on the safe side of their resolution criterion (see their Fig. 14). This boosts our confidence that the properties of the cusps and the evolution we observed at the innermost 20% mass shell is a genuine effect of the complex triaxial structure of the equilibria, and not a numerical artifact due to two-body relaxation.

We also found that steep initial density profiles lead to equilibria with a leveling off in the circular velocity as function of radius. This suggests a run of density in equilibrium $\rho \propto r^{-2}$ for a non-negligible fraction of the mass. This feature was also reported by Hozumi et al. (2000), who approached the problem from the angle of the collision-less Boltzmann equation.

We have observed evolution in time for the innermost region of the equilibrium profiles, such that the small-scale profile shifts away from triaxiality, and toward oblate axisymmetry (see also Theis & Spurzem 1999; Heller 1999). This would certainly impact on the orbital structure of the equilibrium. In a follow-up investigation, we will explore the orbital structure of the equilibria obtained here in details to bridge over with models of triaxial ellipticals based on distribution functions.

ACKNOWLEDGMENTS

REFERENCES

Aarseth, S.J., Lin, D.C. & Papaloizou, J. 1988, ApJ 324, 288
Aguilar, L.A. & Merritt, D. 1990, ApJ 354, 33
Athanassoula, E., Bosma, A., Lambert, J.-C. et al. 1998, MNRAS 293, 369
Athanassoula, E., Fady, E., Lambert, J.C. & Bosma, A. 2000, MNRAS 314, 475
Athanassoula, E., Vozikis, Ch. L. & Lambert, J. C. 2001, A&A 376, 1135
Barnes, J.A. & Hut, P. 1986, Nature 324, 446
Barnes, J.A., Hut, P. & Goodman, J. 1986 ApJ 300, 112
Barnes, J.A. & Hernquist, L. 1992, ARA&A 30, 705
Barnes, J.A. & Hernquist, L. 1996, ApJ 471, 115
Bertin, G. & Trenti, M. 2003, ApJ 584, 729
Binney, J.J. & Tremaine, S.D. 1987, Galactic Dynamics, Princeton: University Press
Binney, J. & Merrifield, M. 1999, Galactic Astronomy, (Princeton: Princeton University Press),
Boily, C.M. 1994, *Homological Flows & Star Formation*, unpublished PhD thesis, Cambridge University
Boily, C.M., Clarke, C.J. & Murray, S.D. 1999, MNRAS 302, 399
Boily, C.M., Athanassoula, E. & Kroupa, P. 2002, MNRAS 332, 971
Burkert, A. 1990, MNRAS 247, 152
Canizzo, J.K. & Hollister, T.C. 1992, ApJ 400, 58
Casertano, S. & Hut, P. 1985, ApJ 298, 80
Curir, A. & Diaferio, A. 1994, A&A 285, 389
Davies, R.L. et al. 1983, ApJ 266, 41
Dehnen, W. 1993, MNRAS 265, 250
Diemand, J., Zemp, M., Moore, B. et al. 2005, MNRAS 364, 665
Fukushige, T. & Makino, J. 1997, 477, L9
Fukushige, T. & Makino, J. 2001, ApJ 557, 533
Fukushige, T., Kawai, A. & Makino, J. 2004, ApJ 606, 625
Funato, Y., Makino, J. & Ebisuzaki, T. 1992, PASJ 44, 613
Gebhardt, K., Richstone, D., Ajhar, E.A. et al. 1996, AJ 112 105
Heller, C.H. 1999, in The Evolution of Galaxies on Cosmological Time-scales, ASP Conference Series Vol. 187, ed. J. E. Beckman & T. J. Mahoney (San Francisco: PASP), 178
Henriksen, R.N. & Widrow, L.M. 1997, Phys. Rev. Lett. 78, 3426
Henriksen, R.N. & Widrow, L.M. 1999, MNRAS 306, 352
Hernquist, L. 1990, ApJ 356, 359
Holley-Bockelmann, K., Mihos, J.C.. Sigurdsson, S. et al. 2001, ApJ 549, 862
Holley-Bockelmann, K., Mihos, J.C., Sigurdsson, S. et al. 2002, ApJ 567, 817
Hozumi, S., Fujiwara, T. & Kan-Ya, Y. 1996, PASJ 48, 503
Hozumi, S., Burkert, A. & Fujiwara, T. 2000, MNRAS 311, 377
Iguchi, O. et al. 2005, Physical Review E 71, 1
Kandrup, H. & Siopis, S. 2003, MNRAS 345, 727
Kawai, A., Fukushige, T., Makino, J., Taiji, M. 2000, PASJ, 52, 659
Laine, S., van der Marel, R.P.. Lauer, T.R. et al. 2003, AJ 125, 478
Lauer, T.R., Ajhar,E.A., Byun, Y.-I. et al. 1995, AJ 110, 2622
LeDelliou, M. & Henriksen, R.N. 2003, A&A 408, 27
Lynden-Bell, D. 1967, MNRAS 136, 101

May, A. & van Albada, T.S. 1984 MNRAS 209, 15

McGlynn, T.A. 1984, ApJ 281, 13

Merrall, T.E.C. & Henriksen, r.N. 2003, ApJ 595, 43

Merritt, D. 1999, PASP 111, 129

Merritt, D. & Cruz, F. 2001, ApJ 551, L41

Merritt, D. & Fridman, T. 1996, ApJ 460, 136

Merritt, D. & Aguilar, L.A. 1985, MNRAS 217, 787

Moore, B., Ghigna, S., Governato, F. et al. 1998, ApJ 524, 19

Moore, B., Kazantzidis, S., Diemand, J., Stadel, J. 2004, MNRAS 354, 522

Nakano, T. & Makino, J. 1999, ApJ 510, 155

Navarro, J.F., Frenk, C.S. & White, S.D.M. 1997, ApJ 490, 493

Navarro, J.F., Hayashi, E., Power, C. et al. 2004, MNRAS 349, 1039

Palmer, P. & Papaloizou, J.C.B. 1987, MNRAS 224, 1043

Perez, J., Alimi, J.-M., Aly, J.-J., et al. 1996, MNRAS 280, 700

Poon, M.Y. & Merritt, D. 2001, ApJ 549, 192

Power, C., Navarro, J.F., Jenkins, A. et al. 2003, MNRAS 338, 14

Press, W.H. et al. 1992, Numerical Recipes in Fortran, 2nd Ed., (Cambridge: Cambridge University Press)

Roy, F. & Perez, J. 2004, MNRAS 348, 62

Teuben, P.J. 1995, in PASP Conf Series Vol. 77, Astronomical Data Analysis Software and Systems IV, ed. R. Shaw, H.E. Payne & J.J.E. Hayes (San Francisco: PASP), p. 398 (see url http://bima.astro.umd.edu/nemo)

Theis, C. & Spurzem, R. 1999, A&A 341, 361

van Albada, T.S. 1982, MNRAS 201, 939

van de Ven, G., Hunter, C., Verolme, E.K. et al. 2003, MNRAS 342, 1056

Table 1. List of runs with cold scale-free initial conditions.

Name	N [10^3]	θ_c	$1/\epsilon$	γ
d001	100	0.7	512	3/2
d004	100	0.6	512	3/2
d003	100	0.5	512	3/2
d002	100	0.4	512	3/2
d005	100	0.3	512	3/2
d006	100	0.2	512	3/2
d019	10	0.4	512	3/2
d010	25	0.4	512	3/2
d008	32	0.4	512	3/2
d009	50	0.4	512	3/2
d020	100	0.4	512	3/2
d022	200	0.4	512	3/2
d023	400	0.4	512	3/2
d007	800	0.4	512	3/2
d011	100	0.4	512	0
d012	100	0.4	512	1/2
d015	100	0.4	512	3/4
d013	100	0.4	512	1
d016	100	0.4	512	5/4
d017	100	0.4	512	7/4
d014	100	0.4	512	2
d031	100	0.4	32	3/2
d030	100	0.4	64	3/2
d025	100	0.4	128	3/2
d024	100	0.4	256	3/2
d021	100	0.4	512	3/2
d026	100	0.4	1024	3/2

Table 2. Morphology of equilibria obtained for runs with different particle number N. The smoothing is $\epsilon = 1/512$ and $\gamma = 3/2$ in all cases. Values are averages over the innermost 80% system mass.

Name	N [10^3]	b/a	c/a	$< \tau_* >$
d007	800	0.76	0.45	0.21
d023	400	0.81	0.47	0.28
d022	200	0.76	0.47	0.20
d002	100	0.78	0.45	0.27
d009	50	0.72	0.48	0.06
d008	32	0.77	0.52	0.12
d010	25	0.78	0.52	0.12
d019	10	0.80	0.57	0.10

Table 3. Morphology of equilibria obtained for runs with different smoothing ϵ. The number of particles is $N = 100,000$ and $\gamma = 3/2$ in all cases. Values are averages over the innermost 80% system mass.

Name	$1/\epsilon$	b/a	c/a	$< \tau_* >$
d031	32	0.65	0.43	-0.03
d030	64	0.70	0.44	0.08
d025	128	0.72	0.44	0.14
d024	256	0.86	0.47	0.38
d021	512	0.70	0.40	0.17
d002	512	0.82	0.55	0.30
d026	1024	0.98	0.56	0.47

Table 4. Morphology of equilibria obtained for runs with different initial power index γ. The smoothing is $\epsilon = 1/512$ and $N = 100,000$ in each case. Values are averages over the innermost 80% system mass.

Name	γ	b/a	c/a	$<\tau_*>$
d012	1/2	0.65	0.48	-0.13
d015	3/4	0.64	0.44	+0.08
d013	1	0.74	0.45	+0.14
d016	5/4	0.71	0.44	+0.10
d002	3/2	0.78	0.45	+0.27
d017	7/4	0.88	0.49	+0.39
d014	2	0.98	0.58	+0.47

Table 5. Parameters of the calculations based on $\gamma = 3/2$ Dehnen models (Eq. 2). The smoothing length is $\epsilon = 1/512$ and $N = 100,000$ in each case.

Name	Q	b/a	c/a	$<\tau_*>$	Comment
h001	0.0	0.98	0.61	0.42	Highly oblate
h009	0.05	0.63	0.52	-0.18	
h002	0.1	0.63	0.62	-0.41	Highly prolate
h008	0.15	0.74	0.73	-0.21	
h003	0.2	0.98	0.96	0.00	(quasi-) spherical
h004	0.4	> 0.98	> 0.98	0.00	spherical